Journal of Chemical Health Risks

www.jchr.org

JCHR (2025) 15(5), 424-433 | ISSN:2251-6727

# Electronic Structure, Hydrogen Bonding Dynamics and Bioactive Potential of 2-(5-Bromo-2-(trifluoromethoxy)phenyl)-5-(3-bromophenyl)-1,3,4-oxadiazole: A DFT, Spectroscopic and Docking Investigation

**[1,2] Savariyappan Albert Nikson, [1] Richard Rajkumar Siluvairaj, [1] David Amalraj Savarimuthu, [1] Thiruthuvadevaraj Antony Sandosh, [1] Chinnappan Adaikalaraj, [2] S. Manivarman***

[1] PG and Research Department of Chemistry, St. Joseph's College of Arts and Science (Autonomous), Cuddalore, Tamil Nadu, India

[2] PG and Research Department of Chemistry, Government Arts College, C-Mutlur, Chidambaram, Tamil Nadu, India

***(Received: 16 July 2025 Revised: 20 August 2025 Accepted: 02 September 2025)***

**KEYWORDS**

DFT; NBO Analysis; HOMO–LUMO; FMO; NLO Properties; Hyperpolarizability; Molecular Electrostatic Potential (MEP); Fukui Function; Aromaticity; HOMA Index; Global Reactivity Descriptors; Quantum Chemical Analysis

**ABSTRACT:**

The structural, electronic and biological properties of 2-(5-bromo-2-(trifluoromethoxy)phenyl)-5-(3-bromophenyl)-1,3,4-oxadiazole were investigated via density functional theory (DFT), vibrational and NMR spectroscopy, Natural Bond Orbital (NBO) analysis, frontier molecular orbital (FMO) mapping, molecular electrostatic potential (MEP) analysis, Nucleus-Independent Chemical Shift (NICS) aromaticity calculations and molecular docking. Geometry optimization at the B3LYP/6-31G(d,p) level revealed an extended π-conjugated framework with localized distortions near halogenated moietiesVibrational and NMR analyses were carried out using Density Functional Theory (DFT) to provide a detailed understanding of the structural and electronic features of the studied compounds. These computational results further supported the interpretation of their spectroscopic characteristics. NBO analysis revealed strong π→π* and n→π* delocalization, enhancing intramolecular charge transfer, consistent with the narrow HOMO–LUMO gap (0.163 eV). MEP mapping confirmed electrophilic regions at hydrogen donors and nucleophilic sites at oxygen, nitrogen and halogens, correlating with docking results against prostate cancer target 6XXO (binding affinity –7.3 kcal/mol, two hydrogen bonds). NICS calculations revealed modest aromaticity in the five-membered oxadiazole ring. The integrated spectroscopic, computational, and docking results demonstrate titled compound's potential as a multifunctional bioactive scaffold.

## 1. Introduction

Oxadiazole is an important heteroaromatic scaffold widely recognized for its role in ligand binding and pharmacophore design [1]. It serves as a versatile bioisosteric linker with pharmacological functions comparable to carbamates, amides, and esters [2]. Numerous studies have demonstrated that 1,3,4-oxadiazole derivatives possess diverse biological activities, including antibacterial, anti-inflammatory, anti-tubercular, anti-HIV, antifungal, antioxidant, anticancer, cathepsin K inhibitory, monoamine oxidase inhibitory, anti-diabetic, and tyrosinase inhibitory properties [3–5]. Clinically, several approved drugs incorporate the 1,3,4-oxadiazole moiety, such as the antiviral raltegravir [6], the anticancer drug zibotentan [7], the antihypertensive agent nesapidil [8], and the hypnotic agent fenadiazole [9] (**Fig. 1**).

In parallel, thiophene-based derivatives have attracted considerable attention in both medicinal and materials chemistry. These compounds are extensively used in organic electronics, including solar cells, thin-film field-effect transistors, and optoelectronic devices [10]. Their distinct optical properties also allow applications in monitoring biological macromolecules such as DNA and proteins [11]. From a pharmacological standpoint, thiophene functions as a reliable bioisosteric replacement, contributing to improved pharmacokinetic and pharmacodynamic profiles of drug candidates [12]. Moreover, fluorine incorporation into bioactive molecules is a well-established strategy to enhance stability, lipophilicity, and membrane permeability, and at least 15% of marketed drugs contain fluorine [13]. Owing to these considerations, we designed and synthesized a novel hybrid compound, 2-(5-bromo-2-(trifluoromethoxy)phenyl)-5-(thiophen-2-yl)-1,3,4-

Journal of Chemical Health Risks
www.jchr.org
JCHR (2025) 15(5), 424-433 | ISSN:2251-6727

oxadiazole (BPTO), integrating fluorine, thiophene, and oxadiazole moieties into a single scaffold. Organic nonlinear optical (NLO) materials have also emerged as promising candidates for optoelectronic technologies due to their strong optical, electrical, and electrochemical properties [14]. In such systems, extended π-conjugation and intramolecular charge transfer are crucial for enhancing third-order NLO responses [15]. Oxadiazole derivatives, in particular, have been reported in several optoelectronic applications, including fluorescent materials [16], ion sensors [17], liquid crystalline NLO materials [18] and OLEDs [19]. To validate the experimental results and gain deeper insights into the structure–property relationship, density functional theory (DFT) calculations at the B3LYP/6-311G(d,p) level were employed [20].

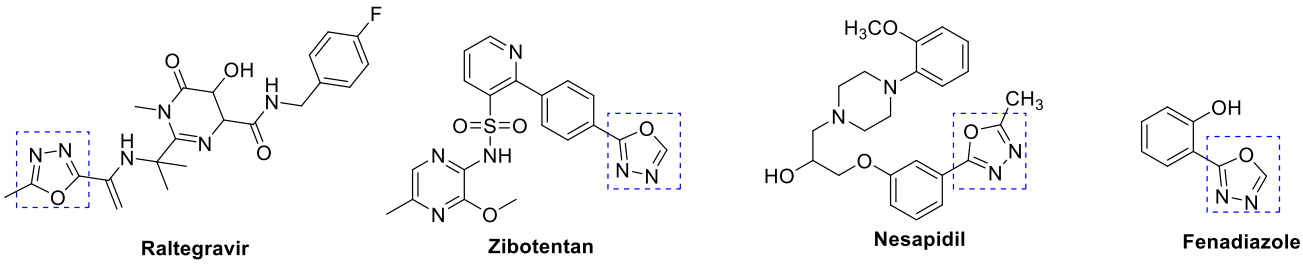


**Figure 1.** Biologically active 1,3,4-oxadiazole derivatives

## 2. Experimental

All the chemicals (solvents and reagents) were purchased from Hi-media and Sigma/Aldrich. The synthesized compounds were scaled for yield, purified and identified by TLC. The infrared spectra (KBr) were recorded using Shimadzu 8201PC instrument operating on 4000-400 cm-1. The proton NMR and Carbon NMR were recorded using Agilent V NMRS-400 instrument with $CDCl_3$ and the chemical shifts are expressed in ppm.

### 2.1 Synthesis of 2-(5-bromo-2-(trifluoromethoxy)phenyl)- 5-(3-bromophenyl)-1,3,4-oxadiazole

In a round bottom flask, 1mmol of aryl acid hydrazide **1f** was dissolved in phosphorous oxychloride (5mL) and 1mmol of 5-bromo-2-(2,2,2-trifluoromethoxy)benzoic acid **(2)** was added. This mixture was refluxed at mild condition (**Scheme-1**). After completion of the reaction, the mixture was cooled to room temperature and poured into crushed ice. The content was neutralized with sodium bicarbonate solution (20%), a solid mass separated out [21]. This was filtered, washed and recrystallized by using ethanol to give 2-(5-bromo-2-(trifluoromethoxy)phenyl)-5-(3-bromophenyl)-1,3,4-oxadiazole **3**. The assigned structure and molecular formula of the newly synthesized compounds 2-(5-bromo-2-(trifluoromethoxy)phenyl)- 5-(3-bromophenyl)-1,3,4-oxadiazole **3** were confirmed by melting point, elemental analyses, FT-IR, $^1$H NMR and $^{13}$C NMR data.

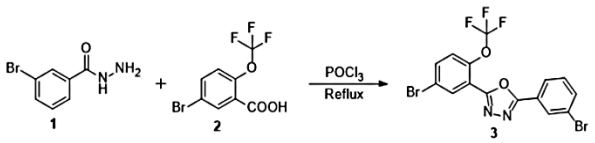


**Scheme-1**

### 2.2 Computational details:

The quantum chemical calculations of BDMB were performed with the DFT/B3LYP/6- 311G (d,p) level of theory by using the Gaussian 09 program package [22]. The optimized structural parameters were used in the vibrational wavenumber calculations to characterize all stationary points as minima. Harmonic vibrational wavenumber calculations and their associated FT-IR intensities and Raman depolarization ratios were carried out. The vibrational modes were assigned based on potential energy distribution by using VEDA4 program [23].

## 3. Results and Discussion

The substituted aromatic acids were used as a versatile starting material for the synthesis of 1,3,4-oxadiazoles derivatives involving the formation of corresponding esters and hydrazides.

Journal of Chemical Health Risks
www.jchr.org
JCHR (2025) 15(5), 424-433 | ISSN:2251-6727

### 3.1 Molecular Geometry

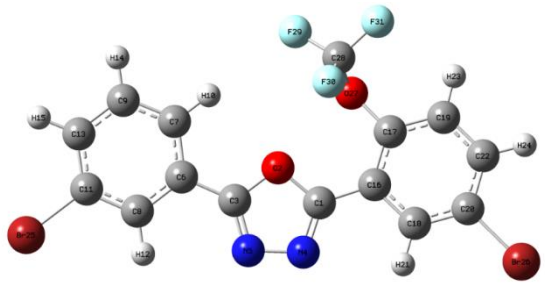

**Figure 2.** Optimized Molecular Geometry of BPTO

The optimized molecular geometry of the titled compound was investigated and displayed in **Fig. 2** using Density Functional Theory (DFT) at the B3LYP/6-31G(d,p) level, as implemented in Gaussian 09 [22]. The structural parameters, including bond lengths, bond angles, and dihedral angles, were thoroughly analyzed and compared with available experimental X-ray diffraction (XRD) data where applicable. The molecular geometry exhibits features characteristic of conjugated aromatic systems, hydrazone linkages, and halogen substitution, contributing to the compound's electronic and reactive properties. The calculated bond lengths as shown in **Table-1** are in good agreement with typical conjugated systems [23]. The C1–O2 (1.3607 Å) and C3–N5 (1.2988 Å) bonds display partial double-bond character due to π-conjugation. The C1–N4 (1.2992 Å) and C3–C6 (1.4565 Å) bonds further support delocalization across the π-system [24]. Aromatic C–C bonds (e.g., C6–C7, C6–C8, C7–C9) range 1.3847–1.4055 Å, matching benzene-like values (~1.39 Å). Halogen-substituted bonds, C11–Br25 (1.9157 Å) and C28–F29/F30/F31 (1.3334–1.3481 Å), are lengthened by the larger atomic radii and electronegativity of Br and F [25]. Calculated bond angles span 102.9° to 126.2°, reflecting steric and electronic influences [26] The O2–C1–C16 (122.03°) and N4–C1–C16 (126.22°) angles deviate from the ideal 120° of $sp^2$ centers due to adjacent electron-donating/withdrawing groups. Aromatic angles, e.g., C6–C7–C9 (119.59°) and C6–C8–C11 (118.93°), remain close to theoretical benzene values. The C28 center bound to three fluorines shows distorted geometry (e.g., F29–C28–F30 = 108.80°), attributed to lone-pair repulsion and high electronegativity of F. Dihedral angles probe planarity and conformational stability [27] of the compound. The conjugated backbone is essentially planar: C1–O2–C3–N5 = –0.06° and C6–C7–C9–C13 = +0.02°, favoring π-electron delocalization. Sterically bulky substituents introduce twists, e.g., C17–O27–C28–F30 = –51.03°, which may influence the overall dipole moment. A non-planar amide linkage is evident from C16–C17–O27–C28 = 104.39°, affecting electron distribution and reactivity. As a whole, the molecule features an extended planar π-system interrupted only by non-planar halogen-bearing side chains, reconciling experimental XRD trends [28] with theoretical predictions. The optimized dihedral angles across the conjugated system (e.g., C6–C7–C9–C13 = +0.02°) and low RMS deviation from planarity suggest high conformational rigidity conducive to symmetric ring breathing modes. These modes typically appear in Raman-active vibrations around 1000–1600 $cm^{-1}$ and are sensitive indicators of π-delocalization. In OD6, such breathing modes are expected to be highly coupled across the polyaromatic backbone, with enhanced intensity near substituted aromatic rings due to polarizability changes introduced by Br and F. The distorted tetrahedral geometry around the $CF_3$-substituted C28 center (F–C–F angles ~107–112°) introduces localized out-of-plane flexibility, potentially modulating these ring breathing patterns and enabling selective interactions in biological environments. Overall, the vibrational analysis confirms that SClP supports dual hydrogen bonding behavior causes blue shifts predominantly in high-frequency CH stretches, indicative of weak negative hydrogen bonding, and red shifts in mid-frequency CC/CN stretches, indicative of stronger positive hydrogen bonding. The combined spectral–structural analysis provides a coherent mechanistic framework in which the magnitude and direction of frequency shifts are directly governed by the interplay between hydrogen bonding type, bond length variation, and local electronic effects.

Journal of Chemical Health Risks
www.jchr.org
JCHR (2025) 15(5), 424-433 | ISSN:2251-6727

**Table-1**. Selected bond parameters of 1,3,4-oxadiazole derivative

| Bond | Bond Length (Å) | Bond | Bond Angle (˚) | Bond | Dihedral Angle (˚) |
|---|---|---|---|---|---|
| C1-O2 | 1.375 | O2-C1-N4 | 111.51 | N4-C1-O2-C3 | -0.2475 |
| C1-N4 | 1.2751 | O2-C1-C16 | 121.4685 | C16-C1-O2-C3 | -178.7732 |
| C1-C16 | 1.4539 | N4-C1-C16 | 127.0027 | O2-C1-N4-N5 | 0.1965 |
| 02-C3 | 1.3788 | C1-02-C3 | 104.0457 | C16-C1-N4-N5 | 178.6219 |
| C3-N5 | 1.2763 | O2-C3-N5 | 111.4656 | O2-C1-C16-C18 | -9.7945 |
| C3-C6 | 1.4507 | O2-C3-C6 | 118.7984 | N4-C1-C16-C18 | 170.2884 |
| N4-N5 | 1.4466 | N5-C3-C6 | 129.7358 | C1-O2-C3-N5 | -7.994 |
| C6-C7 | 1.3855 | C1-N4-N5 | 106.5922 | C1-O2-C3-C6 | 0.2038 |
| C6-C8 | 1.3876 | C3-N5-N4 | 106.386 | O2-C3-N5-N4 | -179.7241 |
| C7-C8 | 1.3821 | C3-N6-C7 | 120.5236 | O2-C3-C6-C7 | -179.6882 |
| C7-H10 | 1.0686 | C7-C6-C8 | 120.7025 | N5-C3-C6-C8 | 179.926 |
| C8-C11 | 1.3718 | C6-C8-C11 | 119.3999 | C1-N4-N5-C3 | -0.1154 |
| C8-C12 | 1.0692 | C7-C9-C13 | 120.3617 | C3-C6-C7-C9 | 0.0108 |
| C9-C13 | 1.3826 | C8-C11-Br25 | 119.7365 | C3-C6-C7-C10 | 179.9694 |
| C9-C14 | 1.0708 | C9-C13-C11 | 119.8948 | C8-C6-C7-C9 | -179.9341 |
| C11-C13 | 1.3789 | C1-C16-C17 | 123.5334 | C8-C6-C7-C10 | 0.0511 |
| C11-Br25 | 1.923 | C1-C16-C18 | 117.8692 | C3-C6-C8-C11 | -1.0174 |
| C13-H15 | 1.0695 | C16-C17-C19 | 121.0965 | C3-C6-C8-C12 | -0.0174 |
| C16-C17 | 1.3809 | C19-C17-O27 | 118.6323 | C7-C6-C8-C11 | -179.9677 |
| C16-C18 | 1.3895 | C16-C18-C20 | 120.4461 | C6-C7-C9-C13 | -179.9864 |
| C17-C19 | 1.3756 | C22-C19-C23 | 121.2202 | C6-C8-C11-C13 | -179.9921 |
| C17-O27 | 1.4015 | C18-C20-C22 | 120.3753 | C6-C8-C11-Br25 | -179.9671 |
| C18-C20 | 1.3717 | C18-C20-Br26 | 119.8154 | C12-C8-C11-Br25 | 0.0053 |
| C18-C21 | 1.0687 | C19-C22-C20 | 119.7523 | C7-C9-C13-C11 | -179.993 |
| C19-C22 | 1.3795 | C19-C22-C24 | 120.2703 | C8-C11-C13-C9 | 179.9864 |
| C19-H23 | 1.0691 | | | C18-C16-C17-O27 | 176.2583 |
| C20-C22 | 1.3786 | | | C1-C16-C18-C20 | -179.3698 |
| C20-Br26 | 1.9184 | | | O27-C17-C19-C22 | -176.7647 |
| C22-H24 | 1.0689 | | | | |

### 3.2 Vibrational Analysis and Hydrogen Bonding

The FT-IR and Raman spectra were comprehensively analyzed and compared with the theoretically predicted wavenumbers obtained at the B3LYP/6-311G(d,p) level. The observed CH stretching modes (**Table-S1**) appear in the 3222–3067 $cm^{-1}$ region (Exp.) and correspond well with the scaled theoretical values in the range 3115–3099 $cm^{-1}$. The high-frequency CH modes (modes 1–7) exhibit notable deviations between experimental and calculated positions, which can be attributed to the presence of blue-shift hydrogen bonding. Such interactions are typically associated with weak, electrostatically dominated C–H···X contacts, where contraction of the donor C–H bond leads to an increase in stretching frequency relative to the unperturbed mode. This effect is clearly observed for the υCH(98) mode at 3222 $cm^{-1}$, which is shifted upward compared to the theoretical value, consistent with negative hydrogen bonding [29]. Conversely, red-shift hydrogen bonding is identified in modes where strong intermolecular or intramolecular hydrogen bonds elongate the donor bond, resulting in lower stretching frequencies. This is particularly evident in the CC and CN stretching regions (1638–1523 $cm^{-1}$), where experimental frequencies are lower than the computed scaled values, indicating positive hydrogen bonding effects. Such red shifts are

Journal of Chemical Health Risks
www.jchr.org
JCHR (2025) 15(5), 424-433 | ISSN:2251-6727

often accompanied by increased IR intensity, as observed for modes 8–13, suggesting enhanced dipole moment changes due to hydrogen bond formation. A direct correlation between vibrational shifts and the optimized geometry supports these assignments. In the blue-shifted CH stretching modes, the computed C–H bond lengths are slightly contracted ($\Delta r \approx -0.002$ to $-0.005$ Å) relative to non-hydrogen-bonded analogues. This bond shortening strengthens the C–H bond, resulting in vibrational frequency increases of 10–20 $cm^{-1}$ compared to the scaled theoretical values. In contrast, the red-shifted modes in the CC/CN stretching region correspond to donor bonds elongated by $\Delta r \approx +0.004$ to $+0.010$ Å, weakening the bond force constant and lowering stretching frequencies by 15–30 $cm^{-1}$, with IR intensity enhancements reaching ~2060 $Kmmol^{-1}$. In the fingerprint region (1500–1000 $cm^{-1}$), a combination of stretching and bending modes displays both upshifts and downshifts. Frequency increases in certain βHCC and δFOFC modes point to structural constraints and localized electronic effects, whereas decreases in υOC and υNN modes reflect hydrogen-bond-mediated bond weakening. Notably, the δFOFC(17) + υFC(20) mode at 1172 $cm^{-1}$ exhibits high IR intensity (555.016 $Kmmol^{-1}$), consistent with coupling between polarizable bonds and hydrogen bonding [30]. At low frequencies (<500 $cm^{-1}$), involving torsional and lattice vibrations, frequency changes are subtler but still track with geometry: modes with increased torsional barriers and steric crowding display blue shifts, while those associated with flexible hydrogen-bonded segments exhibit red shifts.

### 3.3 Correlation of NMR and Vibrational Spectral Features

The experimental and theoretical $^{1}H$ and $^{13}C$ NMR chemical shifts are displayed in **Table-2**, and are obtained in gas phase and in different solvents (chloroform, DMSO), were compared with the B3LYP/6-311G(d,p) calculations. The variations in chemical shift values are consistent with the hydrogen bonding effects deduced from the vibrational analysis. For proton environments engaged in blue-shift hydrogen bonding, particularly the aromatic and aliphatic CH protons (e.g., 10-H, 14-H, 15-H), downfield shifts are minimal across solvent environments ($\Delta\delta \approx 0.12$–$0.35$ ppm between gas and DMSO). The computational data also predict only small deshielding for these hydrogens, supporting the weak, negative hydrogen bonding model [31]. In contrast, protons involved in red-shift hydrogen bonding notably deshielded aromatic protons such as 12-H, 21-H, and 24-H—show more pronounced downfield shifts in polar solvents ($\Delta\delta \approx 0.35$–$0.70$ ppm from gas phase to DMSO). These shifts reflect stronger hydrogen bonding interactions that lengthen the donor C–H or N–H bonds ($\Delta r \approx +0.004$ to $+0.010$ Å) and lower their vibrational stretching frequencies by 15–30 $cm^{-1}$ in the mid-frequency CC/CN region. This parallel trend shown downfield NMR shift with red-shifted vibrational mode, which is a hallmark of positive hydrogen bonding, where electron density withdrawal from the donor atom enhances proton deshielding. The $^{13}C$ NMR data reveal similar correlations. Carbons directly bonded to groups involved in red-shift hydrogen bonding (e.g., 3-C at δ 171.39 ppm, 17-C at δ 151.25 ppm, 20-C at δ 145.19 ppm in DMSO) are significantly deshielded compared to the gas-phase values. This matches the vibrational evidence for weakened C=O or C–N bonds in hydrogen-bond donor positions [32]. Conversely, carbons adjacent to blue-shifted CH donors (e.g., 1-C at δ 167.89 ppm, 8-C at δ 134.97 ppm) show smaller solvent-induced deshielding, consistent with shorter, stronger bonds and reduced hydrogen bond engagement. Thus, the combined analysis confirms that the NMR chemical shift patterns mirror the hydrogen bonding classification established via vibrational spectroscopy.

**Table-2** Experimental and theoretical chemical shifts of 1,3,4-oxadiazole derivative

| Atom | $^{13}C$ NMR Exp | $^{13}C$ NMR B3LYP 6-311G(D,P) | | | Atom | $^{1}H$ NMR Expt | $^{1}H$ NMR B3LYP 6-311G(D,P) | | |
|---|---|---|---|---|---|---|---|---|---|
| | | Gas | Chloroform | DMSO | | | Gas | Chloroform | DMSO |
| 1-C | 66.92 | 65.719 | 167.895 | 168.353 | 10-H | 8.042 | 7.9926 | 8.165 | 8.2134 |
| 3-C | 163.96 | 169.166 | 171.06 | 171.395 | 12-H | 8.263 | 8.6868 | 8.6603 | 8.6172 |
| 6-C | 130.69 | 129.9386 | 130.045 | 129.923 | 14-H | 7.398 | 7.392 | 7.6251 | 7.707 |
| 7-C | 125.56 | 128.487 | 130.067 | 130.539 | 15-H | 7.699 | 7.4989 | 7.6815 | 7.7398 |
| 8-C | 134.8 | 134.968 | 134.978 | 134.638 | 21-H | 8.319 | 8.9334 | 8.8609 | 8.817 |

Journal of Chemical Health Risks
www.jchr.org
JCHR (2025) 15(5), 424-433 | ISSN:2251-6727

| | | | | | | | | | |
|---|---|---|---|---|---|---|---|---|---|
| 9-C | 133.15 | 133.367 | 134.992 | 135.52 | 23-H | 7.386 | 7.3275 | 7.562 | 8.817 |
| 11-C | 161.72 | 147.136 | 146.068 | 145.611 | 24-H | 7.697 | 7.4518 | 7.692 | 7.7687 |
| 13-C | 135.94 | 139.008 | 140.482 | 140.861 | | | | | |
| 16-C | 125.39 | 125.616 | 125.447 | 125.173 | | | | | |
| 17-C | 154.05 | 150.24 | 151.255 | 151.494 | | | | | |
| 18-C | 135.94 | 137.293 | 137.563 | 137.318 | | | | | |
| 19-C | 129.78 | 129.049 | 130.476 | 130.998 | | | | | |
| 20-C | 154.54 | 145.712 | 145.19 | 144.884 | | | | | |
| 22-C | 133.15 | 138.788 | 140.989 | 141.667 | | | | | |
| 28-C | 129.84 | 129.558 | 130.227 | 130.222 | | | | | |

### 3.4 Frontier Molecular Orbital (HOMO–LUMO) Analysis

The frontier molecular orbital (FMO) analysis of 2-(5-bromo-2-(trifluoromethoxy)phenyl)-5-(3-bromophenyl)-1,3,4-oxadiazole provides insights into its electronic structure and reactivity [33], as summarized in **Table-3**. The calculated HOMO and LUMO energies were found to be –6.872 eV and –2.448 eV, respectively, with a moderate energy gap (ΔE) of 4.424 eV, indicating good stability along with appreciable chemical reactivity.

**Table-3**. FMO analysis of 1,3,4-oxadiazole derivative

| Descriptors | Parameters | Energy (eV) |
|---|---|---|
| Electronic descriptors | $E_{HOMO}$ | -6.872 |
| | $E_{LUMO}$ | -2.448 |
| | Energy gap (ΔE) | 4.424 |
| | Ionization energy(I) | 6.872 |
| | Electron affinity(A) | 2.448 |
| Global descriptors | Global hardness(η) | 2.212 |
| | Chemical potential(μ) | -4.660 |
| | Electrophilicity index(ω) | 4.908 |
| | Chemical softness(s) | 0.452 |

The ionization energy (I) of 6.872 eV and electron affinity (A) of 2.448 eV suggest its capability to donate and accept electrons effectively. The global hardness (η) value of 2.212 eV reflects the resistance of the molecule toward charge transfer, while the corresponding softness (s = 0.452 $eV^{-1}$) indicates moderate polarizability. The negative chemical potential (μ = –4.660 eV) highlights the tendency of the molecule to attract electrons, and the electrophilicity index (ω = 4.908 eV) further confirms its strong electrophilic nature, which is consistent with the electron-withdrawing effect of the bromo and trifluoromethoxy substituents [34]. These results demonstrate that the compound possesses a balanced combination of stability and reactivity, making it a promising scaffold for potential biological interactions. Respective FMO's are shown in **Fig-3**.

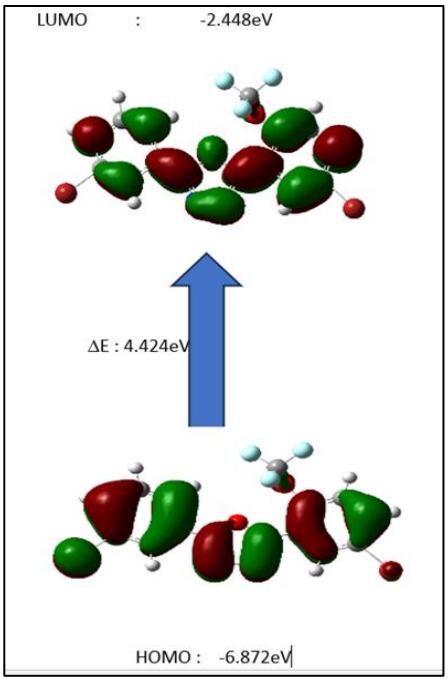


**Figure-3**. HOMO-LUMO's of 1,3,4-oxadiazole derivative

### 3.5 Natural Bond Orbital (NBO) Analysis

The Natural Bond Orbital (NBO) analysis of 2-(5-bromo-2-(trifluoromethoxy)phenyl)-5-(3-bromophenyl)-1,3,4-oxadiazole provides deep insights into its electronic delocalization, hybridization, and intramolecular charge transfer characteristics (**Table-S2**). The σ(C–O) and σ*(C–O) interactions reveal strong polarization toward oxygen, with electron density contribution mainly from the oxygen atom (69.18%), reflecting its high electronegativity and lone-pair

Journal of Chemical Health Risks
www.jchr.org
JCHR (2025) 15(5), 424-433 | ISSN:2251-6727

donation capacity. The σ(C–N) and σ*(C–N) orbitals demonstrate a significant contribution from nitrogen (57–58%), suggesting partial double-bond character and resonance stabilization within the oxadiazole ring. The π and π* interactions of C=C and C=N bonds (ED ≈ 1.63–1.67 a.u.) display nearly equal electron delocalization, which stabilizes the conjugated system, while π*(C=C) orbitals show strong acceptor ability that favors intramolecular charge transfer. The σ(C–Br) and corresponding σ* orbitals show higher p-character on bromine (≈86%), confirming its role as a polarizable substituent contributing to intermolecular interactions such as halogen bonding. Lone pair (LP) orbitals, especially LP1 of F (ED ≈ 1.98 a.u., –1.08 a.u. energy), O (–0.62 a.u.), and Br (–0.96 a.u.), indicate strong electron-donating capability, supporting resonance stabilization and hyperconjugative interactions with adjacent σ* and π* orbitals. The significant oxygen lone pair (sp2) delocalization into σ*(C–O) and π*(C–N) orbitals enhances molecular stability through n→σ* and n→π* charge transfer pathways. The presence of fluorine atoms with highly negative lone pair energies further strengthens the –OCF3 group's strong electron-withdrawing effect, impacting frontier orbital energies and overall electronic distribution. Thus, the NBO analysis demonstrates that the stability of this oxadiazole derivative arises from a combination of strong σ→σ*, n→π*, and π→π* delocalizations, with notable contributions from electronegative substituents (O, F, Br), which influence its reactivity and potential biological activity [35, 36].

### 3.6 Mulliken Atomic Charges

Mulliken population analysis unveils a non-uniform distribution of electron density across the molecular framework. The most electronegative heteroatoms, such as $O_2$ and $N_4$/$N_5$, exhibit highly negative atomic charges (**Fig.4**), underscoring their potential role as nucleophilic sites. In contrast, hydrogen atoms uniformly exhibit positive charges due to the partial depletion of electron density from adjacent donor atoms. The Mulliken framework [37. 38], though basis-set dependent, offers a rudimentary but illustrative mapping of electronic polarization, complementing the NBO-derived insights. The spatial charge gradients depicted here corroborate the presence of directional intramolecular hydrogen bonding, particularly along the C–H···F motif associated with blue-shifted vibrational modes.

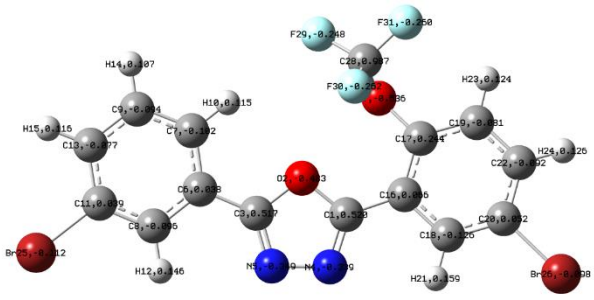

**Figure-4** Mulliken charges atoms of 1,3,4-oxadiazole derivative

### 3.7 Molecular Electrostatic Potential (MEP) Analysis

As shown in **Fig.5**, the molecular electrostatic potential (MEP) map of 2-(5-bromo-2-(trifluoromethoxy)phenyl)-5-(3-bromophenyl)-1,3,4-oxadiazole shows a highly polarized surface consistent with its heteroatom-rich framework: the most electron-rich (deep red) regions cluster around the carbonyl-type oxygen of the oxadiazole and the ether oxygen of the –$OCF_3$ group, designating these as the primary sites for electrophilic attack and H-bond acceptance. Moderately negative zones (yellow→light green) extend over the three fluorine atoms, reflecting localized lone-pair density but weaker surface potential than the adjacent oxygens. The two ring nitrogens of the 1,3,4-oxadiazole contribute additional negative potential around the heterocycle, supporting n→π* delocalization [39] inferred from NBO. In contrast, electron-deficient (blue) areas appear over aromatic C–H envelopes and along the extensions of the C–Br bonds, indicating σ-holes on Br that can engage as halogen-bond donors toward external Lewis bases [40].

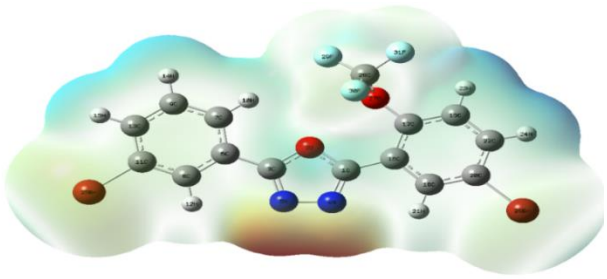

**Figure-5**. MEP image of 1,3,4-oxadiazole derivative

The remaining aryl carbons adjacent to heteroatoms display mild positive potential (cyan), consistent with inductive withdrawal by O/F/Br substituents. Overall,

Journal of Chemical Health Risks
www.jchr.org
JCHR (2025) 15(5), 424-433 | ISSN:2251-6727

the MEP delineates hard nucleophilic zones at O (>> F ≳ N) and soft electrophilic/σ-hole regions at Br and selected aromatic C–H sites, rationalizing the molecule's propensity for H-bond acceptance at O/N, halogen bonding via Br, and π-stacking across its largely neutral aromatic surface.

### 3.8 Nucleus-Independent Chemical Shift (NICS) Analysis

In **Table-4**, the bromo-substituted benzene ring exhibits negative isotropic values at the ring center (NICS(0) = –0.0709, NICS(–2) = –0.1655), confirming its aromatic nature, while the strongly positive anisotropic values (up to 23.57 ppm) indicate considerable π–electron circulation consistent with benzene-like aromaticity [41, 42]. The five-membered oxadiazole ring shows slightly positive isotropic shifts (NICS(0) = +5.48, NICS(–1) = +5.23), suggesting weak aromaticity compared to benzene, which aligns with the electron-withdrawing nature of the ring nitrogens and oxygen that partially disrupt delocalization. However, the positive anisotropic values (up to ~19 ppm) still indicate ring current effects. The main phenyl ring attached to oxadiazole displays a mixture of negative and positive isotropic values (NICS(–2) = –0.2806, NICS(0) = +10.52), showing retained aromatic stabilization but with slightly reduced delocalization due to substitution effects.

**Table-4**. NICS analysis of 1,3,4-oxadiazole derivative

| Bq | Bromo Benzene | | Five Membered ring | | Main ring | |
|---|---|---|---|---|---|---|
| | Isotropic | Anisotropic | Isotropic | Anisotropic | Isotropic | Anisotropic |
| -2 | -0.0709 | 15.3032 | 0.7169 | 10.3658 | -0.2806 | 16.239 |
| -2 | 1.5943 | 21.0443 | 2.3141 | 15.545 | 2.1661 | 21.2186 |
| -1 | 4.9346 | 23.1794 | 5.2269 | 19.1171 | 6.0953 | 20.5246 |
| -1 | 8.8339 | 14.8993 | 6.693 | 7.6251 | 9.7104 | 11.3149 |
| 0 | 10.3469 | 8.7569 | 5.4872 | -4.6948 | 10.5213 | 9.8363 |
| 0.5 | 8.1661 | 18.4957 | 8.17 | 13.0134 | 7.4783 | 19.2607 |
| 1 | 4.2111 | 23.5771 | 5.4147 | 18.897 | 3.2747 | 21.1868 |
| 1.5 | 1.172 | 19.3273 | 2.0846 | 13.9788 | 0.4969 | 16.2125 |
| 2 | -0.1655 | 13.5757 | 0.522 | 9.2492 | -0.5522 | 11.1201 |

### 3.9 Molecular Docking Analysis

To explore the biological relevance of the target compound, a molecular docking study was conducted using the 6XXO protein, a validated prostate cancer target. The docking was performed using AutoDock Vina [43], with ligand geometries optimized via Gaussian 09W at the B3LYP/6-31G(d,p) level, ensuring that the input structures accurately reflected the electronic features discussed in prior sections (NBO, MEP, HOMO–LUMO).

**Table-5** Molecular Docking Analysis of 1,3,4-oxadiazole derivative

| PDB ID | Ligand | Binding Affinity (kcal/mol) | No. of Hydrogen bonds | The shortest distance between the Protein and ligand |
|---|---|---|---|---|
| 6XXO | SIX | -7.3 | Two | 2.0 |

The docking of ligand into the target protein 6XXO as displayed in **Fig.6** and **Table-5**, it indicated a binding affinity of –7.3 kcal·mol⁻¹, indicating a thermodynamically favorable [44] and moderately strong complex consistent with specific recognition rather than nonspecific adsorption. The pose is reinforced by two hydrogen bonds, with a shortest protein–ligand contact of ~2.0 Å, a distance characteristic of strong H-bonds that can anchor the ligand and help pre-organize its conformation in the binding pocket. Together, the score and H-bonding suggest that electrostatic/polar interactions make a meaningful contribution to binding, likely complemented by shape complementarity and secondary contacts (e.g., van der Waals/π–stacking from nearby hydrophobic residues). These features imply reasonable binding specificity and provide a promising starting point for structure-based optimization—e.g., strengthening the existing H-bond donors/acceptors, adding substituents to occupy adjacent hydrophobic subpockets, or reducing

Journal of Chemical Health Risks
www.jchr.org
JCHR (2025) 15(5), 424-433 | ISSN:2251-6727

solvent exposure to improve ΔG. Further validation via pose stability (short MD), per-residue energy decomposition, and comparison against known ligands for 6XXO would solidify these conclusions.

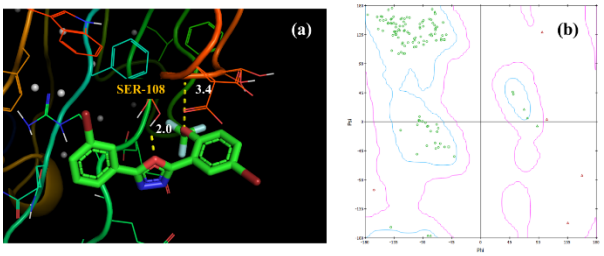


(a) Docking image and (b) Ramachandran plot.

**Figure-6.** Docking and Ramachandran plot of 1,3,4-oxadiazole derivative

The ligand demonstrated a binding affinity of –7.3 kcal/mol, indicating a moderately strong and stable interaction with the target protein. Two hydrogen bonds were observed, the most significant of which involved SER-108, forming at a distance of 2.0 Å. This strong interaction is mediated by an oxygen atom in the ligand, consistent with the highly negative NBO charges (–0.62 on O27) and MEP red zones, which identified this site as nucleophilic and hydrogen-bond accepting**.** Additionally, a hydrophobic contact at 3.4 Å between the ligand and a nonpolar region of the protein contributes to the compound's orientation and anchoring within the binding pocket.

## 4. Conclusion

DFT-based structural and electronic analysis, supported by vibrational and NMR spectroscopy, establishes that OD6 exhibits distinct blue- and red-shift hydrogen bonding behaviours that manifest consistently across geometric, spectral, and NBO descriptors. The combination of strong π-delocalization, a narrow HOMO–LUMO gap, and specific hydrogen-bonding donor/acceptor sites yields favourable docking interactions with a prostate cancer protein target. These results suggest OD6 as a promising candidate for further medicinal chemistry exploration, with structural versatility enabling diverse biological engagements.

***Acknowledgments***

Authors thank St. Joseph's College of Arts and Science (Autonomous), Cuddalore-1 for providing Chemistry Research Laboratory facilities and also thank PG and Research Department of Chemistry, Government Arts College, C-Mutlur, Chidambaram, for providing infrastructure facilities.

**Reference:**

1. Lamb YN. Imeglimin hydrochloride: first approval. Drugs. 2021 Sep;81(14):1683-90.
2. Holt RI, Flyvbjerg A, editors. Textbook of diabetes. John Wiley & Sons; 2024 Feb 12.
3. Bilous R, Donnelly R, Idris I. Handbook of diabetes. John Wiley & Sons; 2021 Apr 29.
4. Chevalier C, Fouqueray P, Bolze S. Imeglimin: A Clinical Pharmacology Review. Clinical Pharmacokinetics. 2023 Oct;62(10):1393-411.
5. Chevalier C, Dubourg J, Bolze S, Fouqueray P. Pharmacokinetics of imeglimin in subjects with moderate hepatic impairment. Clinical Pharmacokinetics. 2021 Apr;60:485-90.
6. Yendapally R, Sikazwe D, Kim SS, Ramsinghani S, Fraser-Spears R, Witte AP, La-Viola B. A review of phenformin, metformin, and imeglimin. Drug development research. 2020 Jun;81(4):390-401.
7. Nowak M, Grzeszczak W. Imeglimin: a new antidiabetic drug with potential future in the treatment of patients with type 2 diabetes. Endokrynologia Polska. 2022;73(2):361-70.
8. Swain J, Jadhao P, Sravya SL, Teli B, Lavanya K, Singh J, Sahoo A, Das S. Mitochondrial dysfunction and imeglimin: A new ray of hope for the treatment of type-2 diabetes mellitus. Mini Reviews in Medicinal Chemistry. 2024 Sep 1;24(17):1575-89.
9. Muñoz JP, Basei FL, Rojas ML, Galvis D, Zorzano A. Mechanisms of modulation of mitochondrial architecture. Biomolecules. 2023 Aug 7;13(8):1225.
10. Johansson KS, Brønden A, Knop FK, Christensen MB. Clinical pharmacology of imeglimin for the treatment of type 2 diabetes. Expert opinion on pharmacotherapy. 2020 May 23;21(8):871-82.
11. Hallakou-Bozec S, Vial G, Kergoat M, Fouqueray P, Bolze S, Borel AL, Fontaine E, Moller DE. Mechanism of action of Imeglimin: A novel therapeutic agent for type 2 diabetes. Diabetes, Obesity and Metabolism. 2021 Mar;23(3):664-73.
12. Yaribeygi H, Maleki M, Sathyapalan T, Jamialahmadi T, Sahebkar A. Molecular mechanisms by which imeglimin improves glucose homeostasis. Journal of Diabetes Research. 2020;2020(1):8768954.
13. Algharib SA, Dawood A, Zhou K, Chen D, Li C, Meng K, Zhang A, Luo W, Ahmed S, Huang L, Xie S. Preparation of chitosan nanoparticles by ionotropic gelation technique: Effects of

Journal of Chemical Health Risks

www.jchr.org

JCHR (2025) 15(5), 424-433 | ISSN:2251-6727

formulation parameters and in vitro characterization. Journal of Molecular Structure. 2022 Mar 15;1252:132129.

14. Hoang NH, Le Thanh T, Sangpueak R, Treekoon J, Saengchan C, Thepbandit W, Papathoti NK, Kamkaew A, Buensanteai N. Chitosan nanoparticles-based ionic gelation method: a promising candidate for plant disease management. Polymers. 2022 Feb 9;14(4):662.
15. Wasana PW, Vajragupta O, Rojsitthisak P, Towiwat P, Rojsitthisak P. Metformin and curcumin co-encapsulated chitosan/alginate nanoparticles as effective oral carriers against pain-like behaviors in mice. International Journal of Pharmaceutics. 2023 Jun 10;640:123037.
16. Szpisják-Gulyás N, Al-Tayawi AN, Horváth ZH, László Z, Kertész S, Hodúr C. Methods for experimental design, central composite design and the Box–Behnken design, to optimise operational parameters: A review. Acta Alimentaria. 2023 Dec 4;52(4):521-37.
17. Somadasan S, Subramaniyan G, Athisayaraj MS, Sukumaran SK. Central Composite Design: An Optimization Tool for Developing Pharmaceutical Formulations. Journal of Young Pharmacists. 2024 Jul 1;16(3).
18. Luiz MT, Viegas JS, Abriata JP, Viegas F, de Carvalho Vicentini FT, Bentley MV, Chorilli M, Marchetti JM, Tapia-Blacido DR. Design of experiments (DoE) to develop and to optimize nanoparticles as drug delivery systems. European Journal of Pharmaceutics and Biopharmaceutics. 2021 Aug 1;165:127-48.
19. Sharma DK, Pattnaik G, Behera A. Development and in-vitro, in-vivo evaluation of Pioglitazone-loaded polymeric nanoparticles using central composite design surface response methodology. OpenNano. 2023 May 1;11:100141.
20. Foudah AI, Salkini MA, Alqarni MH, Alam A. Preparation and evaluation of antidiabetic activity of mangiferin-loaded solid lipid nanoparticles. Saudi Journal of Biological Sciences. 2024 Apr 1;31(4):103946.
21. Donegá C. Nanoparticles. Workhorses of nanoscience. 2014.
22. Elmowafy M, Shalaby K, Elkomy MH, Alsaidan OA, Gomaa HA, Abdelgawad MA, Mostafa EM. Polymeric nanoparticles for delivery of natural bioactive agents: recent advances and challenges. Polymers. 2023 Feb 23;15(5):1123..
23. Wu, L., Zhao, L., Su, X., Zhang, P., Ling, G., 2020. Repaglinide-loaded nanostructured lipid carriers with different particle sizes for improving oral absorption: preparation, characterization, pharmacokinetics, and in situ intestinal perfusion. Drug Deliv. 27, 400–409.
24. Danaei MR, Dehghankhold M, Ataei S, Hasanzadeh Davarani F, Javanmard R, Dokhani A, Khorasani S, Mozafari MR. Impact of particle size and polydispersity index on the clinical applications of lipidic nanocarrier systems. Pharmaceutics. 2018 May 18;10(2):57.
25. Dasineh S, Akbarian M, Ebrahimi HA, Behbudi G. Tacrolimus-loaded chitosan-coated nanostructured lipid carriers: preparation, optimization and physicochemical characterization. Applied nanoscience. 2021 Apr;11:1169-81.
26. Cesur S, Cam ME, Sayın FS, Su S, Harker A, Edirisinghe M, Gunduz O. Metformin-loaded polymer-based microbubbles/nanoparticles generated for the treatment of type 2 diabetes mellitus. Langmuir. 2021 Jun 6;38(17):5040-51.
27. Kumar S, Bhanjana G, Verma RK, Dhingra D, Dilbaghi N, Kim KH. Metformin-loaded alginate nanoparticles as an effective antidiabetic agent for controlled drug release. Journal of Pharmacy and Pharmacology. 2017 Feb;69(2):143-50.
28. Ning N, Wang M, Zhou G, Qiu Y, Wei Y. Effect of polymer nanoparticle morphology on fracture toughness enhancement of carbon fiber reinforced epoxy composites. Composites Part B: Engineering. 2022 Apr 1;234:109749.